Solar Physics
DOI: 10.1007/●●●●●-●●●-●●●-●●●●-●

Comparing coronal densities and large-scale structure between solar rotational tomography and global 3D magnetohydrodynamic simulations

Liam T. Edwards[1] · **Huw Morgan**[1]

© The author(s) ●●●●

Abstract This study compares coronal electron density maps obtained from solar rotational tomography and the Magnetohydrodynamic Algorithm outside a Sphere (MAS) 3D global model. The study spans the length of an entire solar activity cycle from March 2007 until late 2023. The dependence of the electron densities on latitude and heliocentric height are compared, with densities comparing best at the equatorial regions and lower heliocentric heights. The streamer and non-streamer regions are compared separately, as well as the average width of the streamer belt over the duration of solar cycle 24. The MHD model densities typically contain more fine-scale detail than the tomography but there is a very good overall agreement in structure and location of high-density features between both sets of densities. The tomography densities are most accurate in the polar regions since the MHD model uses photospheric magnetogram input which is unreliable at the poles due to projection effects. Due to the current prevalence of MHD models in the research field, the accuracy and reliability of these models is most crucial, with comparisons such as this study highlighting their advantages and disadvantages as well as stressing the importance of solar rotational tomography techniques to help place constraints upon both current and future models.

Keywords: Magnetic fields; Corona, Models, Magnetohydrodynamics, Solar Cycle; Models, Observations

1. Introduction

The outer atmosphere of the sun - the corona - is a tenuous, hot ($> 10^6$ K) plasma consisting of electrically charged ions. As a result, it is optically thin in

✉ L.T. Edwards
lie6@aber.ac.uk
H. Morgan
hum2@aber.ac.uk

[1] Department of Physics, Aberystwyth University, Ceredigion, Cymru, SY23 3BZ, UK

the visible light (VL) and extreme-ultraviolet (EUV) spectral regimes resulting in observations of a point on the plane-of-sky (POS) including contributions from along the line-of-sight (LOS) through the medium. Observations of the VL corona are therefore 2D projections of a more complex 3D underlying structure. One of the most effective techniques used to determine the 3D distribution of the coronal plasma in those spectral regimes is tomography. It involves observing the sun/corona from different viewpoints which can be achieved by observing the corona over a time period of rotation. This period should span half a solar rotation, although this period may be shortened by using two or more viewpoints. For comprehensive overviews of SRT and stereoscopic techniques see Vásquez (2016) and Aschwanden (2011).

SRT techniques have been used extensively since their inception by Altschuler and Perry (1972) with many studies improving upon this original method. For example, Frazin (2000) and Frazin and Janzen (2002) developed a more robust method for tomographic inversion from a time series of VL images. Frazin et al. (2007) presented the first 3D tomographic reconstructions of the coronal electron density from an extended sequence of polarized brightness (pB) observations. The study used 2 weeks of images from the Large Angle and Spectrometric Coronagraph (LASCO) (Brueckner et al., 1995) on board the Solar and Heliospheric Observatory (SOHO) (Domingo, Fleck, and Poland, 1995). Morgan, Habbal, and Lugaz (2009) presented the Qualitative Solar Rotational Tomography (QSRT) technique which uses total brightness VL observations processed with a suitable background subtraction and a Normalizing Radial Graded Filter (NRGF). The method was used to create global maps of the coronal structure at heliocentric heights $\geq 3\ R_{\odot}$. One key assumption is common in all the aforementioned studies which is that of a static corona during the observation period. This assumption holds particularly during periods of lower solar activity, but breaks down with increasing activity. Butala et al. (2010) presented the first global reconstruction of the corona using a novel dynamic reconstruction method, with Vibert et al. (2016) introducing several new techniques to reduce the effects of coronal dynamics on VL tomographic reconstructions. A novel tomographic technique based on spherical harmonics was developed by Morgan (2019, hereafter Paper II) which is discussed in more detail in section 2.2. More recent studies involving tomographic techniques to study the solar corona include Asensio Ramos (2023) who investigated the application of neural fields for tomographic reconstructions of the corona using data from LASCO/C2.

The coronal plasma is typically constrained and shaped by magnetic field lines, originating from deep within the sun, which permeate throughout the corona and produce the variety of structures and phenomena observed. It is therefore crucial to understand the coronal magnetic field in order to be able to better understand the morphology, properties, and dynamics of the extended solar atmosphere. However, unlike the photosphere where the magnetic fields are routinely measured, it is very difficult to directly measure the magnetic fields in the corona. As a result, theoretical models are required which use the photospheric magnetic field as an inner boundary to simulate the coronal magnetic field configuration. Different techniques have been developed to model the coronal magnetic field based on photospheric magnetic field lower boundary

conditions. The simplest approach is the Potential Field Source Surface (PFSS) model first developed by Schatten, Wilcox, and Ness (1969) and Altschuler and Newkirk (1969). Assuming zero electrical currents in the corona, PFSS models compute the magnetic field in the region from the photosphere to a specified "source surface" where the magnetic field is assumed to be purely radial (typically a heliocentric height of 2.5 $R_\odot$). Due to its simplicity, it is the most commonly used method to model the coronal magnetic field but there are other models, such as 3D global magnetohydrodynamic (MHD) models, which are computationally more expensive and should provide more accurate results due to including the effects of the plasma on the magnetic field. However, it is also common for studies to use a combination of different models (Nedal et al., 2023). Typically, global MHD models can be summarized in two steps: firstly, the photospheric radial magnetic field is used as the lower boundary condition of the model and, secondly, the model advances until the coronal plasma and magnetic fields reach a near-equilibrium. However, there are many different methods of producing MHD models which have been used to study various dynamic phenomena, for example, coronal mass ejections (Mayank et al., 2024; Linker et al., 2023; Török et al., 2018; Lionello et al., 2013), solar energetic particles (Palmerio et al., 2024; Li et al., 2021; Linker et al., 2019; Schwadron et al., 2014), and flares (Agarwal, Bhattacharyya, and Yang, 2024; González-Servín and González-Avilés, 2024; Inoue and Bamba, 2021; Muhamad et al., 2017).

Tomographic and stereoscopic techniques are commonly used in conjunction with MHD models to validate the models and places further constraints on the coronal plasma. Furthermore, since tomographic reconstructions are based purely on coronal observations, whereas MHD models are primarily based upon photospheric magnetic field observations, the former is a more realistic representation of the coronal structure. Vásquez et al. (2008) demonstrated a validation of two 3D MHD coronal models by comparing density outputs from the models with SRT for a single Carrington rotation (CR 2029). Jin et al. (2012) performed a similar validation study using a three-dimensional, two-temperature, Alfvén-wave-driven global solar wind model and electron density derived from a tomographical inversion of LASCO/C2 data. Kramar et al. (2014) used a tomographic reconstruction of the 3D coronal electron density from STEREO/COR1 data during a deep minimum in 2008 (CR 2066) to relate the reconstructed 3D density to open/closed magnetic-field structures. Badman et al. (2022) investigate constraining global coronal models, namely PFSS, Wang-Sheeley-Arge (WSA), and the Magnetohydrodynamic Algorithm outside a Sphere (MAS) models, with multiple independent observables such as EUV observations of coronal hole locations, VL Carrington maps of the streamer belt, and in situ measurements by the Parker Solar Probe and spacecraft at 1 AU.

The structure of this study is as follows: section 2 summarises the MHD model (2.1) and SRT technique (2.2) used in this study, section 3 disseminates the results of the different comparisons between the model and SRT density maps for various physical parameters such as latitude (3.2), heliocentric height (3.3), and isolating the streamer (3.4) and non-streamer (3.5) regions. The study is concluded in section 4.

2. Method

2.1. MAS MHD Model

The MHD model used in this study is the Magnetohydrodynamic Algorithm outside a Sphere (MAS) code developed by Predictive Sciences Inc.[1] (Mikić et al., 1999) which is the main model in the *Corona-Heliosphere* (CORHEL) collection of MHD models (Riley et al., 2012). The package is designed to model the global solar corona from the upper chromosphere out to Earth orbit with the coronal model extending from 1 - 30 $R_\odot$ and the heliospheric model extending from 30 - 215 $R_\odot$. This particular model has been used extensively to model various coronal structures and dynamics (Török et al., 2018; Lionello et al., 2013; Linker et al., 2011) as well as forward modelling to predict the topology of the solar corona during total solar eclipses (Mikić et al., 2018, 2007, 2000).

The model takes photospheric magnetogram data as the lower boundary condition and extrapolates the magnetic field. It can use input data from several observatories including the Mount Wilson Observatory[2], Michelson Doppler Imager[3] on SOHO, and HMI (Scherrer et al., 2012) on the Solar Dynamics Observatory (Pesnell, Thompson, and Chamberlin, 2012). The code uses a non-uniform staggered grid which allows it to resolve smaller-scale structures like active regions, while also allowing for coarser grid points over the global scale. Model runs can be requested on the Community Coordinated Modeling Center[4]. ~~For simplicity~~, these model results are based on a specific Carrington rotation, i.e. the photospheric magnetic field synoptic map used as an input for the model run is built up from a sequence of observations centered at central meridian over a 27-day period. This inner boundary condition is then supplemented with auxiliary boundary conditions that approximate the plasma density and temperature. Consequently, synthetic observables such as pB and B can be calculated to compare the simulation results with observations.

Figure 1 compares VL observations of the 21 August 2017 TSE (*left panel*) with the MAS MHD prediction of the pB (*middle panel*) and coronal magnetic field configuration (*right panel*), showing good qualitative similarities between the observation and the model. In particular, the polar plumes seen in the southern hemisphere in the observation align with those predicted in the pB of the magnetic field configuration. However, despite the overall agreement between the model and observation, the pseudostreamer seen in the north-west region of the observational data is missing in both the predicted pB and magnetic field configuration. This is due to the use of older magnetic field measurements in that region at the time of the eclipse, after which the authors re-ran the simulation with newer observations which did eventually support the formation of the pseudostreamer.

---

[1] https://www.predsci.com/~~portal/home.php~~

[2] https://www.mtwilson.edu/

[3] http://soi.stanford.edu/

[4] https://ccmc.gsfc.nasa.gov/

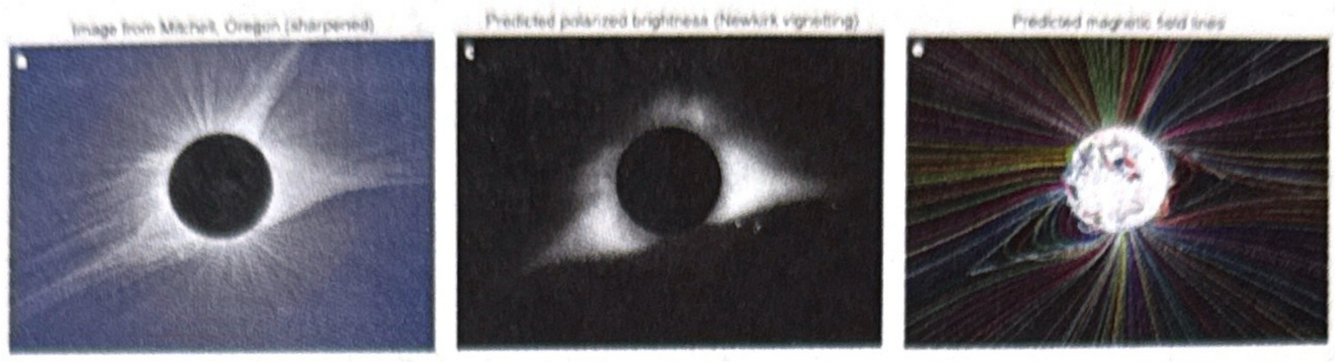


Figure 1. Comparison between VL observation of the 21 August 2017 TSE (*left*) with the MAS MHD prediction of the pB (*middle*) and the magnetic field configuration (*right*), adapted from Mikić et al. (2018)

There are two main model types available: thermodynamic and polytropic. The polytropic models are a 3D MHD model which use a simple energy equation with a reduced adiabatic index (γ) whereas the thermodynamic models use a more sophisticated energy equation which includes coronal heating, radiative losses, and thermal conduction. The thermodynamic models use one of two heating models: heating model 1 or heating model 2. Both are an empirical coronal heating model but the former, described in Lionello et al. 2009, has three components tailored for active regions, coronal holes, and the quiet sun where the volumetric heating relies solely on the local parameters of the magnetic field. The latter, heating model 2, features multiple components designed to match the multi-spectral emission of the corona, much like heating model 1, but in this case the volumetric heating depends on the properties of the surface magnetic field as well.

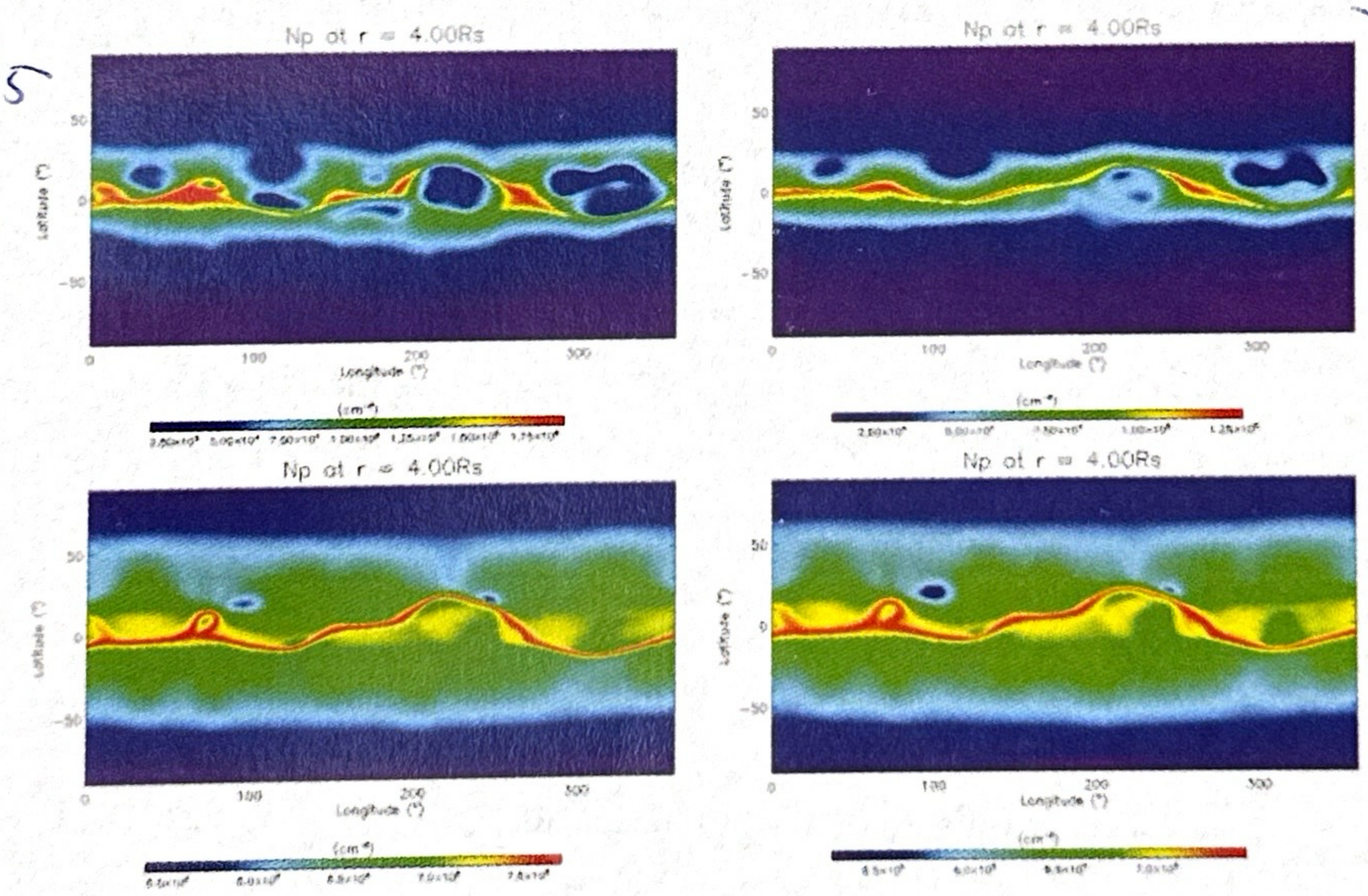


Figure 2. MAS model outputs for a mid-date of 14 December 2008 at a heliocentric height of 4 $R_\odot$. *Upper left:* MAS model output 1. *Upper right:* MAS model output 2. *Bottom left:* MAS model output 3. *Bottom right:* MAS model output 4 (see Table 1 for details on each model).

Figure 2 shows a comparison between different MAS model outputs for a mid-date of 14 December 2008 at a heliocentric height of 4 $R_{\odot}$. The top row show the outputs when using the thermodynamic model with heating model 1 (*left*) and 2 (*right*), whereas the bottom row show outputs when the polytropic model is used. Each model type is described in more detail in Table 1. Density maps were compared for each solar cycle phase (see Table 2) and the resulting MHD output which most closely resembled the tomography in both numerical value and structure was selected for this study. In the case of Figure 2, the model selected for comparison with the tomography density map was model 2 (*top right*). Table 2 shows the model parameters used in this study along with the dates corresponding to each solar cycle phase. The thermodynamic model has been used for each case study with the majority using heating model 2. However, heating model 1 was used for both the minimum and ascending phases of the solar cycle as they more closely resembled the tomography density maps for those phases. Figure 2 gives only a qualitative comparison, whereas quantitative comparisons are much sparser in the field since there are no constraints above the photosphere. Solar rotational tomography techniques can provide these constraints and is one of the few ways in which this can be done globally. This study aims to provide this assessment of empirical global MHD models, where results from the MAS model are qualitatively compared with those acquired using the tomography method, as well as observational data from coronagraphs. Several physical parameters were varied, namely latitude, heliocentric height, and solar cycle phase, along with a comparison between the streamer and non-streamer regions.

Table 1. MAS parameters available for 14 December 2008

Model Number	Observatory	Model Type	Heating Model
1	MDI	Thermodynamic	1
2	MDI	Thermodynamic	2
3	MDI	Polytropic	N/A
4	MDI	Polytropic	N/A

Table 2. MAS parameters for each solar cycle phase

Phase	Date	Observatory	Model Type	Heating Model
Minimum	14/12/2008	MDI	Thermodynamic	1
Ascending	14/08/2011	HMI	Thermodynamic	1
Maximum	14/04/2014	HMI	Thermodynamic	2
Descending	13/02/2017	HMI	Thermodynamic	2
TSE	14/12/2020	HMI	Thermodynamic	2

2.2. Solar Rotational Tomography

Morgan (2015, hereafter Paper I) presents a description of data preprocessing and calibration techniques for the LASCO C2 instrument on SOHO and the SECCHI COR2 instrument aboard STEREO A and B spacecraft. These processed and calibrated coronagraph data are then used as the input for a novel SRT method based on spherical harmonics, presented in Paper II, which reconstructs the coronal electron density. This method is used to obtain density maps of the coronal electrons at heliocentric distances from $\approx 3\ R_\odot$ to $8\ R_\odot$. Maps are produced at ≈ 2 day increments, starting at a mid-date of 17 March 2007, resulting in thousands of maps which can be freely downloaded from the Aberystwyth University archive[5]. Initial results of the method are presented in Morgan and Cook (2020, hereafter Paper III) as well as further developments to the method. The method requires around half a solar rotation (≈ 2 weeks) of COR2A data to produce one coronal density map therefore each map is a static reconstruction of $\pm$ 1 week of observational data from the mid-date. For each mid-date, a set of nine maps are created at heliocentric distances between 4 and $8\ R_\odot$ at $\approx 0.5\ R_\odot$ increments. An example of one of these tomography density maps is shown in Figure 3 for a mid-date of 7 June 2017 and a heliocentric height of $4\ R_\odot$.

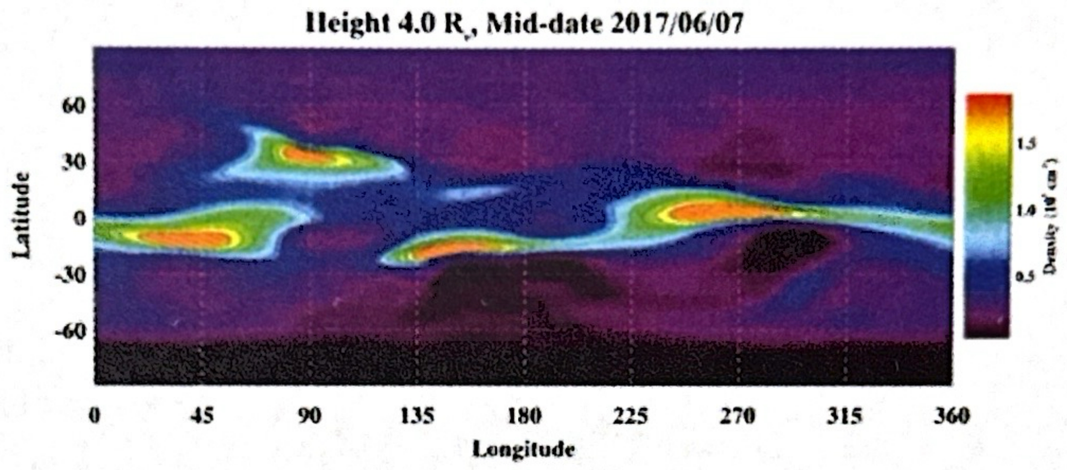


Figure 3. Example of a coronal electron density map formed using the spherical harmonic basis approach of Paper II. The map shows the density at a heliocentric height of 4.0 $R_\odot$ for a mid-date of 7 June 2017 in Carrington longitude-latitude coordinates.

3. Results

3.1. General Comparison

Figure 4 shows a comparison of coronal electron density maps produced using tomography (*left column*) and the MAS model (*right column*) at a heliocentric distance of 4 $R_\odot$ for dates during each phase of the solar activity cycle. The maps span the entirety of solar cycle 24 (2008 - 2019) and the start of solar cycle

[5] https://solarphysics.aber.ac.uk/Archives/tomography/cor2a/

25 (2020) with each phase separated by ≈ 3 years. The minimum phase of solar cycle 25 coincided with the TSE on December 14 2020 thus to avoid confusion with the minimum of solar cycle 24, this minimum phase is labelled as the TSE phase.

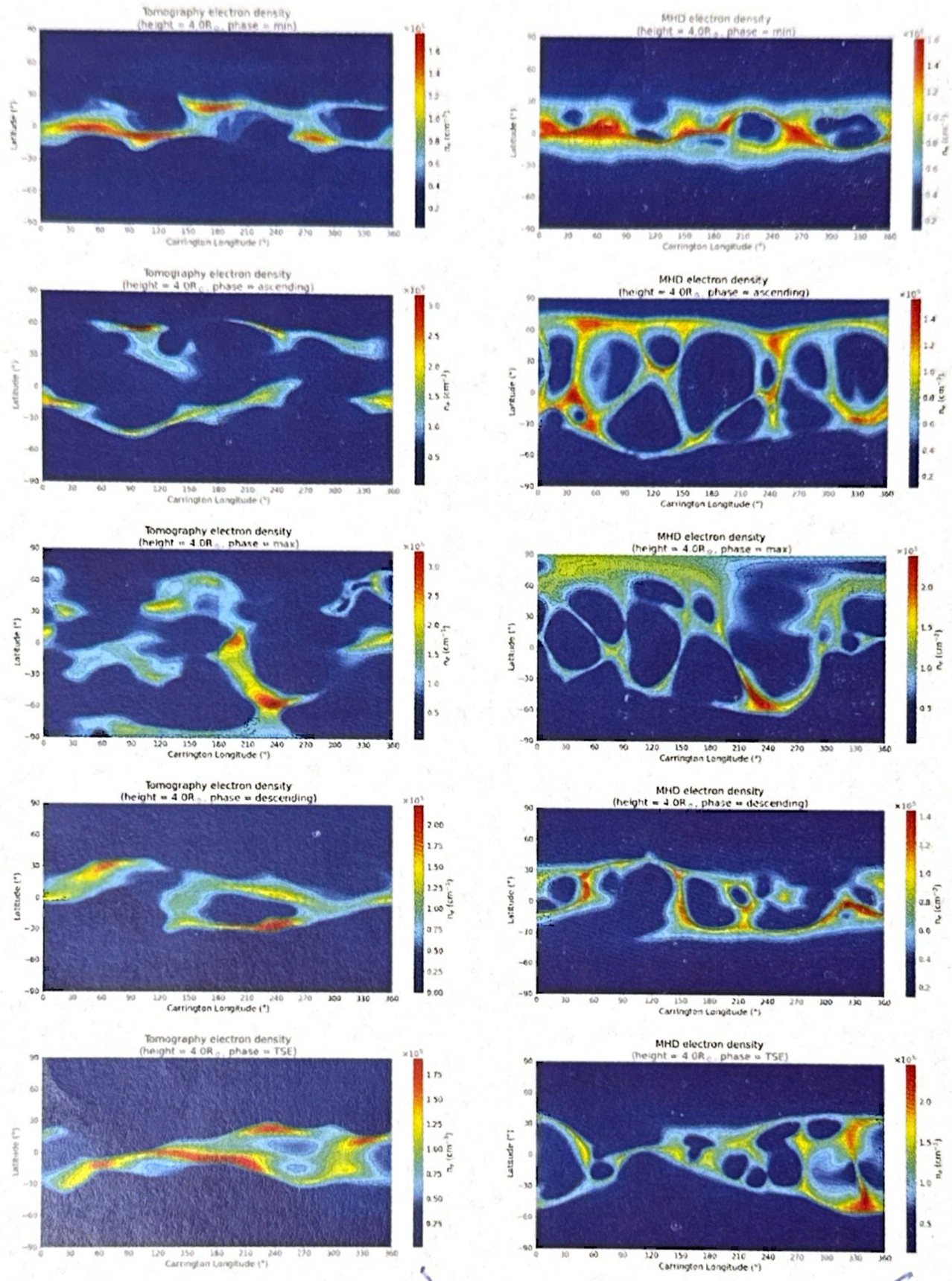


Figure 4. Coronal electron densities produced using tomography (*left column*) and the MAS model (*right column*) at a heliocentric height of 4 $R_\odot$ for dates during each phase of the solar activity cycle - see Table 2 (*top to bottom*: *minimum*, *ascending*, *maximum*, *descending*, *TSE*).

Just in case you don't mention it later:
Important to discuss how MHD maps built for obs of photospheric field @ central meridian (dataset 1) whereas tomography for limb obs (dataset 2)
How are they related? where do they diverge the most? ⇒ That's where disagreement should break down (SOL Min q(cm))

① different regions
② different scales
have a delta scale here

Figure 4 shows that there is good overall agreement between the tomography and the MAS model maps. Despite the fact that the tomography process involves regularization which may remove finer-scale details which are visible in the MAS outputs, the overall structure of maps are very similar. For example, the current sheet, which is more apparent at periods of lower solar activity, can be traced in both the tomography and MAS outputs at similar locations. Furthermore, pockets of lower density regions can be seen in similar locations in both outputs, for example, at solar minimum between 20 and -10° in latitude there are two pockets of lower density at Carrington longitudes of ≈ 210 to 240° and ≈ 300 to 350° in both outputs.

Despite the numerical values of the densities generally agreeing in both the tomography and MAS model outputs, there are times when they do not. For example, during the ascending phase, the upper limit of the tomography's densities ($\approx 3.0 \times 10^5$ cm^{-3}) is double that of the MHD model ($\approx 1.5 \times 10^5$ cm^{-3}). This is counter-intuitive since higher densities would be expected in MHD model output because they show the finer-scale detail whereas the tomography maps are likely smoothed which should result in lower densities than the MHD model. Secondly, both the tomography and MAS outputs show the varying of the streamer belt's width as a function of solar cycle phase very well, with the streamer belt narrower and more contained at times of lower solar activity and much wider and less defined at times of higher solar activity. However, the widths of the streamer belts in the MHD model do not always agree with those of the tomography maps. An example of this difference can be seen during the TSE phase in Figure 4 (bottom row) where the MHD model shows a much wider streamer belt, particularly between 0 - 60° and 270 - 360° Carrington longitude. Finally, despite the regularization in the tomography maps, they show much more detail in the polar regions in comparison to the MAS output. Since the MAS model takes observational measurements of the radial component of the photospheric magnetic field (B_r), usually in the form of line-of-sight photospheric magnetogram, as its input, it cannot accurately measure B_r at higher latitudes due to projection effects. Therefore, it uses a fitting procedure to estimate B_r in the polar regions which is likely why the MAS outputs appear much smoother in the polar regions than the tomographic equivalent.

The third row from the top in Figure 4 shows a tomography map (*left*) and the equivalent MAS model output (*right*) for the same date during solar maximum. As expected, the MAS model output shows much finer-scale structure than the tomography but there is a good agreement in the position of higher density structures and lower density pockets between the two maps. For example, the high density structure at ≈ -30 to -60° latitude and ≈ 210 to 240° longitude is agreed upon very well in both maps, with some obvious discrepancies in the polar regions. For example, the tomography map indicates that there is a relatively high density structure visible in the southern polar region, extending from ≈ 30 to 240° in longitude at a latitude of ≈ -80°, which is not at all visible in the MAS output.

Figure 5 shows VL images from the LASCO C2 instrument aboard SOHO taken over a period of three weeks in April 2014. Since the tomography method requires a minimum of half a Carrington rotation (≈ 14 days) of observation to

create one density map, for a feature to appear in the resulting maps it should be present and fairly stable over this period. In this case, the streamer seen near the south pole at a position angle of $\approx 158°$ (measured counter-clockwise from the north pole) on 7 April 2014 (*left*) can be seen in the coronagraph data a week later on 14 April (*middle*) at position angle $\approx 171°$. It can also be seen on 21 April (*right*) at position angle $\approx 174°$, and the streamer is visible in the tomography map.

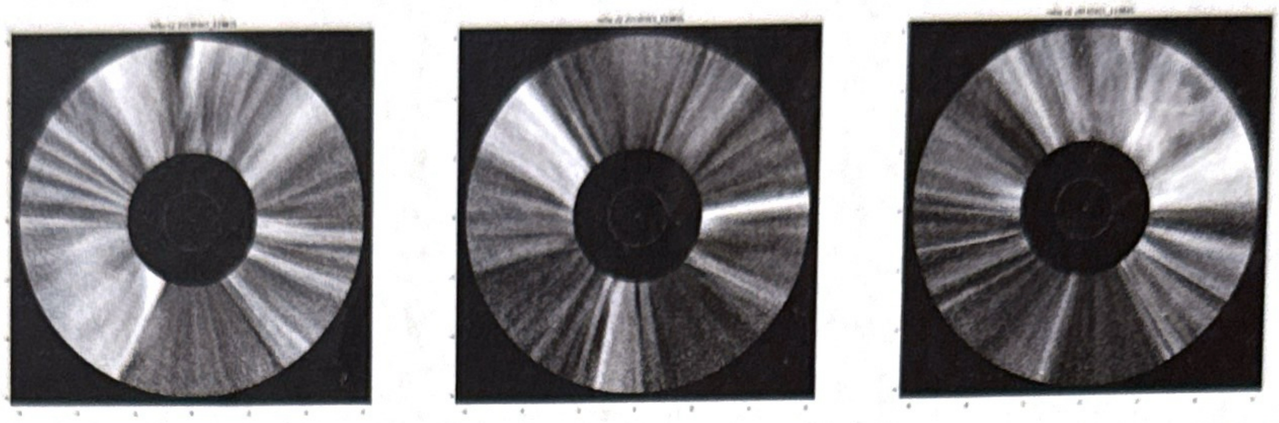


Figure 5. LASCO C2 observations of the VL corona on 7 April 2014 (*left*), 14 April 2014 (*middle*), and 21 April 2014 (*right*) with the streamer of interest seen in the south-eastern region of the lower corona in all three images. To enhance structural detail, the images have been processed with the Normalizing Radially Graded Filter (Morgan, Habbal, and Woo, 2006) and Multiscale Gaussian Normalization (Morgan and Druckmüller, 2014).

Figure 6 shows both the observed and reconstructed polarized brightness of the solar corona at a heliocentric height of 4 $R_\odot$ and a mid-date of 14 April 2014. The observed pB is the parameter upon which the tomography maps are based, whereas the reconstructed pB is the calculated density of the tomography map. Despite a very active corona at the time of observation, the tomography method holds up well in a qualitative comparison. Figure 7 shows a line profile comparison between the observed and reconstructed pB taken at the mid-date of Figure 6 shown as black and red profiles, respectively. The reconstructed pB from the tomography agrees very well with the observed pB, particularly in the southern polar region where the streamer is present. There is a relatively good agreement between the observed and reconstructed pB at position angles of $\approx 90°$ and ≈ 300 - $330°$, as well as at $\approx 180°$ where the streamer of interest is present. However, the pB peak at a position angle of $\approx 45°$ has not been well reconstructed by the tomography method. Despite this, the tomography has accurately represented the true coronal pB, whereas the MHD model has failed to do so in the context of the south polar streamer.

3.2. Latitudinal Comparison

Figure 8 shows a comparison of coronal electron densities derived from the tomography map and the MAS model averaged over longitude for each latitude bin for heliocentric heights of 4 (*top*) and 8 $R_\odot$ (*bottom*). There is a reasonably good agreement between the tomography and the model at the two heights both in terms of the numerical values of the densities in the streamer belt, and the position of the peaks. However, at a heliocentric height of 4 $R_\odot$, the MHD

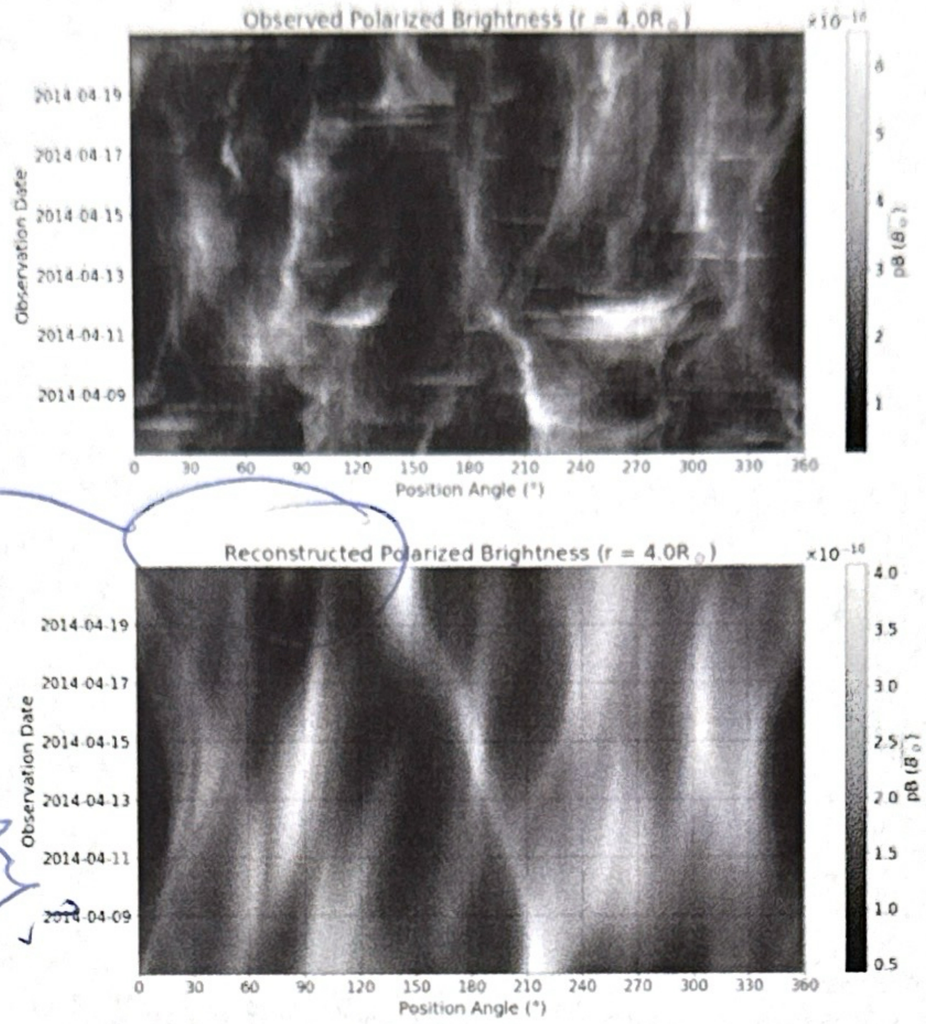


Figure 6. Observed (*top*) and reconstructed (*bottom*) pB maps of the corona at a heliocentric height of 4.0 $R_\odot$ at a mid-date of 14 April 2014. The data are expressed in units of mean solar brightness and are shown as functions of position angle counter-clockwise from solar north.

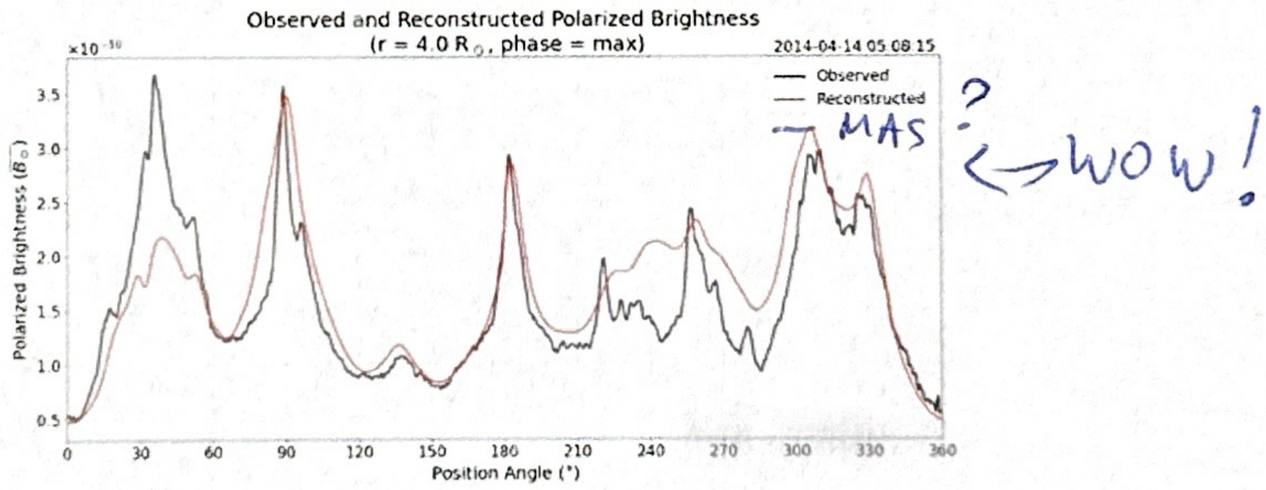


Figure 7. Line profile comparisons of the observed (*black*) and reconstructed (*red*) pB of the corona at a heliocentric height of 4.0 $R_\odot$ taken at a mid-date of 14 April 2014. The data are expressed in units of mean solar brightness and are shown as functions of position angle counter-clockwise from solar north.

densities are typically greater than those given by the tomography whereas, at 8 $R_\odot$, the tomography densities are greater than the MHD model densities. This is particularly apparent in the polar regions where the densities agree well between the two methods at 4 $R_\odot$, but differ greatly at 8 $R_\odot$. The tomography polar

densities at 8 $R_\odot$ are consistent between both poles at $\approx 0.8 \times 10^4$ cm^{-3}, whereas the corresponding densities calculated by the MHD model have a much steeper gradient from each pole towards the equator than the tomography densities. The MHD polar densities are also much lower at this heliocentric height when compared with the tomography ($\approx 0.2 \times 10^4$ at latitudes of $\pm$ 90°). This could be a result of the interpolation method used by the model to estimate the magnetic field in the polar regions due to the difficulty in acquiring observations at higher latitudes. In fact, the tomography should be most accurate at the poles since the LOS of the coronagraph used by the method observes the polar pB almost continually in its entirety. At more central latitudes, parts of the equatorial plane are hidden behind the sun and thus produce data gaps. The MHD model densities are clearly decreasing too rapidly with increasing radial height which is discussed further in later sections. The red and blue shaded regions represent the standard deviations for the tomography and MHD model, respectively, and although there is an agreement in the shape of shaded regions, they are clearly offset both in density and latitude. The MHD standard deviations exhibit a single peak structure, whereas the tomography standard deviations have a double peak structure at 4 $R_\odot$. However, at 8 $R_\odot$, the MHD standard deviations exhibit the same single-peak structure whereas the tomography has three peaks with the left and central peaks seeming to form a double Gaussian shape.

Figure 9 shows densities from both the tomography (*red*) and MAS model (*blue*) averaged along each latitude for each phase of the solar cycle along with their respective standard deviations (*shaded regions*) at 4 $R_\odot$. The two outputs agree well at solar minimum then, as the activity in the solar cycle increases, the outputs differ more. The tomography maps are not as accurate during periods of increased solar activity since the method of producing the maps includes a step which removes signals from coronal mass ejections which occur more frequently at solar maximum. Furthermore, rapid changes in the coronal large-structure also affect the effectiveness of the tomography method (Edwards et al., 2022; Morgan, 2011a,b), as well as causing similar problems with the MHD model, even in the absence of CMEs. There is a large discrepancy in the poles during solar maximum where the tomography estimates a much higher density in the south pole and a much lower density in the north pole, whereas the MHD model estimates the opposite. Despite this, both methods generally produce similar results even during solar maximum.

3.3. Height Dependence

Figure 10 shows the average electron density using tomography (*left column*) and the MAS model (*right column*) as a function of increasing heliocentric height for each phase of the solar cycle, averaged over all longitudes and latitudes. The tomography densities gradually increase from solar minimum to maximum and then decrease towards the TSE phase around the minimum of the next solar cycle. The same pattern is seen in the MHD model output but to a much lesser extent than the tomography. The MHD density at 4 $R_\odot$ during the solar minimum phase is $\approx 0.45 \times 10^5$ cm^{-3} and only increases to $\approx 0.55 \times 10^5$ cm^{-3} at solar maximum. However, the tomography density at 4 $R_\odot$ during solar

Not sure how useful this is as a dataset for comparing models

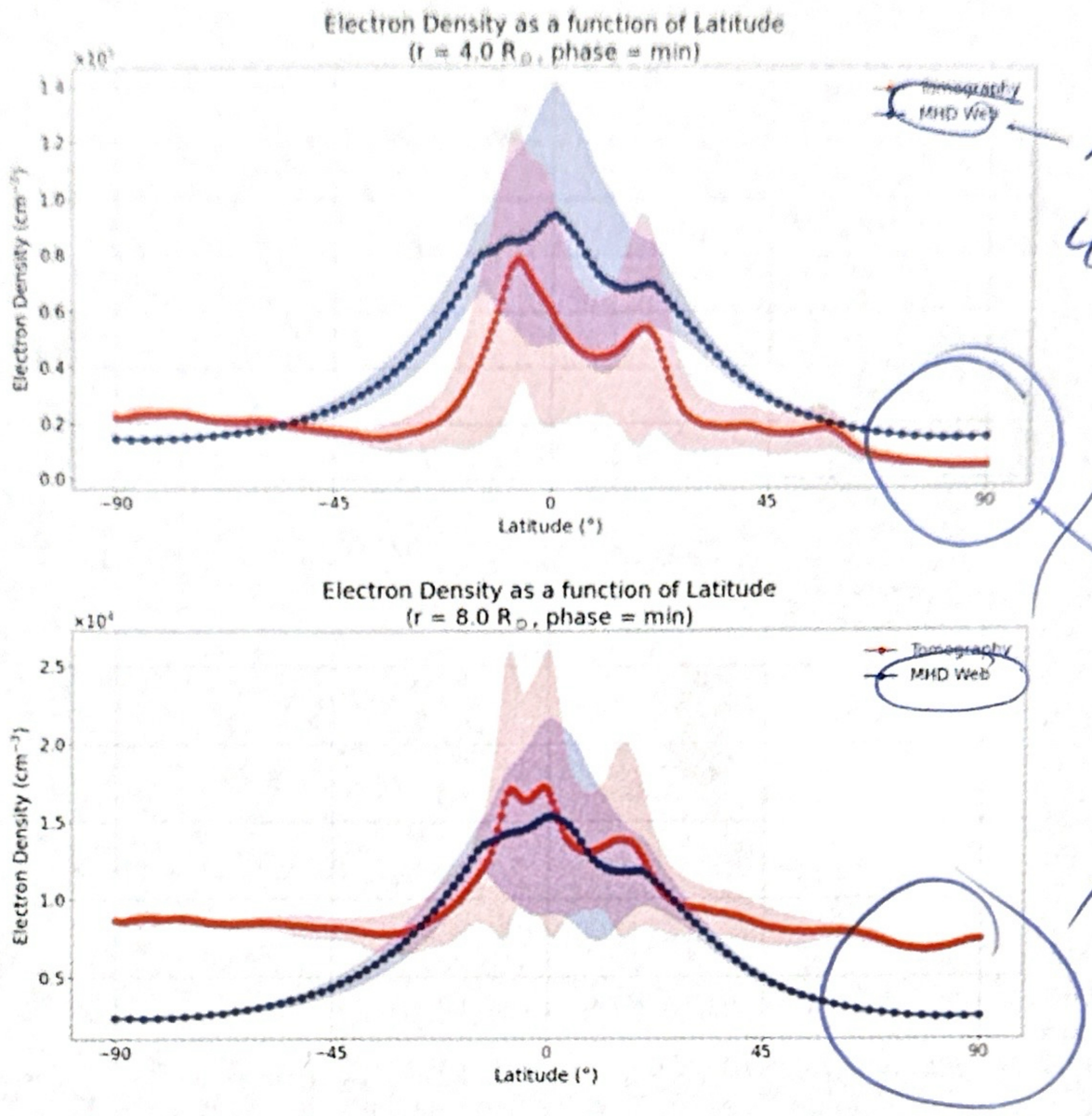


Figure 8. Electron densities derived from the tomography maps (*red*) and MAS model (*blue*) averaged across all longitudes for each latitude for heliocentric heights of 4 (*top*) and 8 $R_\odot$ (*bottom*) during the solar minimum phase (see Table 2) and the red and blue shaded areas represent the tomography and MAS model standard deviations, respectively.

minimum is $\approx 0.25 \times 10^5$ cm^{-3} and increases to $\approx 0.65 \times 10^5$ cm^{-3} during solar maximum. This is due to the activity in the corona increasing, higher-density structures appear more frequently and consequently the average coronal electron density increases.

The average densities from the tomography decrease smoothly as radial height increases at each phase of the solar activity cycle, with the steepest gradient occurring at solar maximum and a much shallower gradient at solar minimum. However, the MHD model results show a more disjointed decrease in global average density as a function of increasing heliocentric height, particularly from 4 to 5 $R_\odot$. This disjoint manifests itself as a steeper gradient between radial heights of 4.5 to 5 $R_\odot$than that between 4 to 4.5 and 5 to 5.5 $R_\odot$. This steepening of the gradient at these heights is seen at each phase of the solar cycle and is most prevalent during solar maximum. Furthermore, the standard deviations, given by the coloured shaded region in each plot, are generally much greater in the MHD model compared to the tomography, particularly during solar minimum. However, the standard deviation of the tomography during solar maximum is

greater which may be expected since the tomography is less reliable during periods of increased solar activity. It is difficult to explain these discrepancies in the MHD model by looking at the global average density alone since the distribution of the streamers and coronal holes can affect the average densities. In the following sections, the corona is separated into streamer and non-streamer regions.

3.4. Streamer Belt

Figure 11 shows a comparison of density maps for the high-density streamer belt region at a heliocentric height of 4 $R_\odot$ for various phases of the solar activity cycle. The streamer belt is defined as any part of the tomography map where the density is greater than 1.5 times that of the average global density which isolates the streamer belt very well in each tomography map. As the solar cycle progresses, the structure of the streamer belt becomes less coherent and more complex before becoming more coherent once again by the end of the cycle. As mentioned previously in section 1, there is a discrepancy between the width of the streamer belt in some instances, primarily in the TSE phase (bottom row) which is seen in this figure. However, despite the discrepancies, the streamer belts given by the tomography and MHD model generally show very good agreement. For example, at solar maximum, there is a high-density feature between -20 to -60° latitude and 200 to 280° Carrington longitude which is seen in both outputs with a very similar numerical value as well as a remarkably similar positional structure. This is a surprising result given the tomography method is generally less accurate during solar maximum.

Figure 12 shows the average streamer densities using tomography (*left column*) and the MAS model (*right column*) as a function of increasing heliocentric height for each phase of the solar cycle. Both methods produce densities which are lower during solar minimum and higher at solar maximum, but the tomography average at 4 $R_\odot$ fluctuates much more than its equivalent MHD density. The densities of the MHD streamers are much higher than those of the tomography at each stage of the cycle, for example, during solar minimum, the average MHD streamer density at 4 $R_\odot$ is $\approx 1 \times 10^5$ cm^{-3} whereas the average tomography streamer density is much lower at $\approx 0.7 \times 10^5$ cm^{-3}. During solar maximum, the average tomography streamer density is greater ($\approx 1.4 \times 10^5$ cm^{-3}) compared to the MHD streamer density ($\approx 1.1 \times 10^5$ cm^{-3}). The unusually steep gradient between 4.5 and 5 $R_\odot$ is also clearly visible at all phases of the solar cycle in the MHD model streamer densities. This phenomena is more apparent in the MHD streamer densities than in the average global densities seen in Figure 10. The percentage difference between the minimum and maximum average streamer densities across the solar cycle at 4 $R_\odot$ is $\approx 67\%$ for the tomography outputs and $\approx 40\%$ for the MHD model which supports the fact that the tomography density at 4 $R_\odot$ varies more across the cycle than its MHD equivalent.

Figure 13 gives two examples of tomography maps where the average streamer belt width is also shown. The top panel shows a density map for a mid-date of 21 March 2007, corresponding to solar minimum, whereas the bottom panel shows a density map for a mid-date of 19 April 2014, corresponding to solar maximum.

The dashed white lines show the average streamer belt width in each case which are determined by calculating the maximum and minimum latitudes of the belt at each longitude and computing their average. The difference between these two average values gives the average width of the streamer belt for that particular tomography map. As expected, the streamer belt is narrower and more coherent at solar minimum than at solar maximum with far fewer high-density features seen outside the dashed white lines than at solar maximum. The calculated average width of the streamer belt is a more accurate representation at times of lower solar activity.

This average streamer belt width was calculated for every tomography map available between 2007 and 2022 as well as each MHD model output obtained for each solar cycle phase studied. The corresponding result of this comparison is shown in Figure 14 where the blue and black data points represent the average streamer belt width at that date from the tomography and MHD model output, respectively. The shaded region and the error bars represent the standard deviation for the tomography and MHD model output widths, respectively. As expected, the average streamer belt width is at its widest in 2014 at the peak of the solar activity cycle and is narrowest at solar minimum. The data gap from early 2014 to late 2015 is as a result of the STEREO-A COR2 outage. The solar cycle trend is apparent. The MHD streamer belt widths agree well with the tomography widths with all data points and their errors overlapping for each solar cycle phase. The same solar cycle trend seen in the tomography is also seen in the MHD model outputs where the streamer belt is narrower and more coherent at periods of lower solar activity, and wider with greater standard deviations at periods of increased activity.

3.5. Non-Streamer Regions

Figure 15 shows the non-streamer regions given by both the tomography (*left*) and the MHD model (*right*), where the data shown are less than or equal to 1.5 times the mean global electron density for that phase of the solar cycle. These results show considerably more discrepancies between them in comparison to those acquired for the streamer belts. The density maps for times of lower solar activity seem relatively similar, but those for solar maximum, for example, are very different. One key difference to note is at solar minimum (*top row*) where the MHD model suggests more uniform and homogeneous densities at higher latitudes, most probably as a result of the aforementioned interpolation procedure used to a lack of quality magnetogram data at high latitudes. The tomography seems to suggest far more variation and finer-scale features than the MHD model.

Figure 16 shows the average non-streamer densities using tomography (*left column*) and the MAS model (*right column*) as a function of increasing heliocentric height for each phase of the solar cycle. Similar to Figure 12, both methods produce densities which are lower during solar minimum and higher at solar maximum, but the tomography average densities are lower than the MHD average densities at each stage of the solar cycle. During solar minimum, the average MHD non-streamer density at 4 $R_{\odot}$ is $\approx 2.5 \times 10^4$ cm^{-3} whereas

the equivalent average tomography density is much lower at $\approx 1.4 \times 10^5$ cm^{-3}. During solar maximum, however, the average tomography non-streamer density at 4 $R_\odot$ is yet again greater ($\approx 3.5 \times 10^4$ cm^{-3}) when compared to the MHD non-streamer density ($\approx 2.9 \times 10^4$ cm^{-3}). The disjoint in the gradient between 4.5 and 5 $R_\odot$ is clearly visible at all phases of the solar cycle in the MHD model non-streamer densities, and is much steeper and more apparent for non-streamer regions. As with the streamer densities, this phenomena is more apparent in the MHD densities. The discrepancy between the tomography and MHD outputs is much greater in the non-streamer regions than the streamer regions. In fact, the average MHD non-streamer densities vary little across the solar cycle from its minimum to maximum value ($\approx$ 14% difference) whereas the tomography average densities vary more ($\approx$ 88% difference).

general comment about Sect 3 is that its mixing in "results" with interp, what and go in Sect 4

Discuss n A

4. Conclusions – develop more +

Disc →

The motivation for this study was to provide a comparison between coronal electron density maps produced using the MAS MHD model and a solar rotational tomography technique. The MAS model that agreed best with the tomography was the thermodynamic model which was to be expected since it uses a more sophisticated energy equation than the polytropic model, including coronal heating, radiative losses, and thermal conduction. Generally, there is good agreement between the density maps produced using the tomography method and those produced using the MAS MHD model. However, there are some cases where the tomography maps show features which are not visible in the MHD outputs, particularly towards higher latitudes ($\varphi \geq \pm 80°$). This can be explained by two reasons; firstly, the tomography method is most accurate at the poles since there is uninterrupted observations along the LOS through both polar regions. The second reason originates from the difficulty in obtaining any meaningful magnetic field observations of the solar poles which consequently affects the ability of MHD models to extrapolate the polar magnetic fields. The densities produced using the tomography method can be verified using the observed and reconstructed pB which agree well throughout the solar cycle. The densities produced by the two methods typically agree well over a solar cycle but there are more discrepancies between the two during periods of increased solar activity. There is also a disagreement in polar densities as heliocentric height increases, with the MHD model densities decreasing too quickly compared with the tomography densities. The tomography densities decreases smoothly as a function of radial height whereas the MHD densities decrease somewhat smoothly but with a sudden sharpening of the gradient between 4.5 and 5 $R_\odot$ across the solar cycle. This sharpening of the density gradient is seen in the global average density as well as in the average density of both the streamer and non-streamer regions - where it is particularly apparent in the non-streamer regions. There is a good overall agreement between the tomography and MHD model outputs for the streamer regions and the average width of the streamer belt agrees well between the two methods. The streamer belt is narrow and more coherent in the density maps at periods of lower solar activity and widens to cover a broader latitude

+ ① Summary Paragraph
② Sources of error (Both models) ← pull from Sect 3
③ Discuss – you have that.
④ Future ideas to pursue?
⑤ conclus...

range during solar maximum and this trend is also seen in the MHD outputs. As mentioned previously, global 3D MHD models play an important role in helping our understanding of solar phenomena, both in the short and long term. As a result, the accuracy and reliability of these models is most crucial, with comparisons such as this study highlighting their advantages and disadvantages as well as stressing the importance of observational techniques to help place physically derived constraints upon both current and future models.

Acknowledgments The STEREO/SECCHI project is an international consortium of the Naval Research Laboratory (USA), Lockheed Martin Solar and Astrophysics Lab (USA), NASA Goddard Space Flight Center (USA), Rutherford Appleton Laboratory (UK), University of Birmingham (UK), Max-Planck-Institut für Sonnen-systemforschung (Germany), Centre Spatial de Liege (Belgium), Institut Optique Théorique et Appliqúee (France), and Institut d'Astrophysique Spatiale (France).

Author Contribution L.E. wrote the main manuscript text and performed the majority of the data analysis and processing. H.M. contributed expertise to the data analysis and reviewed the manuscript.

Funding We acknowledge studentship funding from the Coleg Cymraeg Cenedlaethol to Aberystwyth University that made this work possible.

Data Availability Coronal electron densities obtained using by solar roational tomography can be downloaded from https://solarphysics.aber.ac.uk/Archives/tomography/. The Magnetohydrodynamic Algorithm outside a Sphere (MAS) Model was developed by Predictive Science Inc (https://www.predsci.com/corona/model_desc.html).

Declarations

Conflict of interest The authors declare that they have no conflicts of interest.

References

Agarwal, S., Bhattacharyya, R., Yang, S.: 2024, Study of Reconnection Dynamics and Plasma Relaxation in MHD Simulation of a Solar Flare. *Sol. Phys.* **299**, 15. DOI. ADS.

Altschuler, M.D., Newkirk, G.: 1969, Magnetic Fields and the Structure of the Solar Corona. I: Methods of Calculating Coronal Fields. *Sol. Phys.* **9**, 131. DOI. ADS.

Altschuler, M.D., Perry, R.M.: 1972, On Determining the Electron Density Distribution of the Solar Corona from K-Coronameter Data. *Sol. Phys.* **23**, 410. DOI. ADS.

Aschwanden, M.J.: 2011, Solar Stereoscopy and Tomography. *Living Reviews in Solar Physics* **8**, 5. DOI. ADS.

Asensio Ramos, A.: 2023, Tomographic Reconstruction of the Solar K-Corona Using Neural Fields. *Sol. Phys.* **298**, 135. DOI. ADS.

Badman, S.T., Brooks, D.H., Poirier, N., Warren, H.P., Petrie, G., Rouillard, A.P., Nick Arge, C., Bale, S.D., de Pablos Agüero, D., Harra, L., Jones, S.I., Kouloumvakos, A., Riley, P., Panasenco, O., Velli, M., Wallace, S.: 2022, Constraining Global Coronal Models with Multiple Independent Observables. *Astrophys. J.* **932**, 135. DOI. ADS.

Brueckner, G.E., Howard, R.A., Koomen, M.J., Korendyke, C.M., Michels, D.J., Moses, J.D., Socker, D.G., Dere, K.P., Lamy, P.L., Llebaria, A., Bout, M.V., Schwenn, R., Simnett, G.M., Bedford, D.K., Eyles, C.J.: 1995, The Large Angle Spectroscopic Coronagraph (LASCO). *Sol. Phys.* **162**, 357. DOI. ADS.

Butala, M.D., Hewett, R.J., Frazin, R.A., Kamalabadi, F.: 2010, Dynamic Three-Dimensional Tomography of the Solar Corona. *Sol. Phys.* **262**, 495. DOI. ADS.

Domingo, V., Fleck, B., Poland, A.I.: 1995, The SOHO Mission: an Overview. *Sol. Phys.* **162**, 1. DOI. ADS.

Edwards, L., Kuridze, D., Williams, T., Morgan, H.: 2022, A Solar-cycle Study of Coronal Rotation: Large Variations, Rapid Changes, and Implications for Solar-wind Models. *Astrophys. J.* **928**, 42. DOI. ADS.

Frazin, R.A.: 2000, Tomography of the Solar Corona. I. A Robust, Regularized, Positive Estimation Method. *Astrophys. J.* **530**, 1026. DOI. ADS.

Frazin, R.A., Janzen, P.: 2002, Tomography of the Solar Corona. II. Robust, Regularized, Positive Estimation of the Three-dimensional Electron Density Distribution from LASCO-C2 Polarized White-Light Images. *Astrophys. J.* **570**, 408. DOI. ADS.

Frazin, R.A., Vásquez, A.M., Kamalabadi, F., Park, H.: 2007, Three-dimensional Tomographic Analysis of a High-Cadence LASCO-C2 Polarized Brightness Sequence. *Astrophys. J. Lett.* **671**, L201. DOI. ADS.

González-Servín, M., González-Avilés, J.J.: 2024, Numerical MHD simulations of solar flares and their associated small-scale structures. *Mon. Not. R. Astron. Soc.*. DOI. ADS.

Inoue, S., Bamba, Y.: 2021, An MHD Modeling of the Successive X2.2 and X9.3 Solar Flares of 2017 September 6. *Astrophys. J.* **914**, 71. DOI. ADS.

Jin, M., Manchester, W.B., van der Holst, B., Gruesbeck, J.R., Frazin, R.A., Landi, E., Vasquez, A.M., Lamy, P.L., Llebaria, A., Fedorov, A., Toth, G., Gombosi, T.I.: 2012, A Global Two-temperature Corona and Inner Heliosphere Model: A Comprehensive Validation Study. *Astrophys. J.* **745**, 6. DOI. ADS.

Kramar, M., Airapetian, V., Mikić, Z., Davila, J.: 2014, 3D Coronal Density Reconstruction and Retrieving the Magnetic Field Structure during Solar Minimum. *Sol. Phys.* **289**, 2927. DOI. ADS.

Li, G., Jin, M., Ding, Z., Bruno, A., de Nolfo, G.A., Randol, B.M., Mays, L., Ryan, J., Lario, D.: 2021, Modeling the 2012 May 17 Solar Energetic Particle Event Using the AWSoM and iPATH Models. *Astrophys. J.* **919**, 146. DOI. ADS.

Linker, J.A., Lionello, R., Mikić, Z., Titov, V.S., Antiochos, S.K.: 2011, THE EVOLUTION OF OPEN MAGNETIC FLUX DRIVEN BY PHOTOSPHERIC DYNAMICS. *The Astrophysical Journal* **731**, 110. DOI. https://dx.doi.org/10.1088/0004-637X/731/2/110.

Linker, J.A., Caplan, R.M., Schwadron, N., Gorby, M., Downs, C., Torok, T., Lionello, R., Wijaya, J.: 2019, Coupled MHD-Focused Transport Simulations for Modeling Solar Particle Events. In: *Journal of Physics Conference Series*, *Journal of Physics Conference Series* **1225**, 012007. DOI. ADS.

Linker, J., Torok, T., Downs, C., Caplan, R., Titov, V., Reyes, A., Lionello, R., Riley, P.: 2023, CORHEL-CME: An Interactive Tool For Modeling Solar Eruptions. *arXiv e-prints*, arXiv:2311.03596. DOI. ADS.

Lionello, R., Downs, C., Linker, J.A., Török, T., Riley, P., Mikić, Z.: 2013, Magnetohydrodynamic Simulations of Interplanetary Coronal Mass Ejections. *Astrophys. J.* **777**, 76. DOI. ADS.

Lionello, R., Downs, C., Linker, J.A., Török, T., Riley, P., Mikić, Z.: 2013, MAGNETOHYDRODYNAMIC SIMULATIONS OF INTERPLANETARY CORONAL MASS EJECTIONS. *The Astrophysical Journal* **777**, 76. DOI. https://dx.doi.org/10.1088/0004-637X/777/1/76.

Mayank, P., Vaidya, B., Mishra, W., Chakrabarty, D.: 2024, SWASTi-CME: A Physics-based Model to Study Coronal Mass Ejection Evolution and Its Interaction with Solar Wind. *Astrophysical Journal, Supplement* **270**, 10. DOI. ADS.

Mikić, Z., Linker, J.A., Schnack, D.D., Lionello, R., Tarditi, A.: 1999, Magnetohydrodynamic modeling of the global solar corona. *Physics of Plasmas* **6**, 2217. DOI. ADS.

Mikić, Z., Linker, J.A., Riley, P., Linello, R.: 2000, Predicting the Structure of the Solar Corona During the 11 August 1999 Total Solar Eclipse. In: Livingston, W., Özgüç, A. (eds.) *Last Total Solar Eclipse of the Millennium*, *Astronomical Society of the Pacific Conference Series* **205**, 162. ADS.

Mikić, Z., Linker, J.A., Lionello, R., Riley, P., Titov, V.: 2007, Predicting the Structure of the Solar Corona for the Total Solar Eclipse of March 29, 2006. In: Demircan, O., Selam, S.O., Albayrak, B. (eds.) *Solar and Stellar Physics Through Eclipses*, *Astronomical Society of the Pacific Conference Series* **370**, 299. ADS.

Mikić, Z., Downs, C., Linker, J.A., Caplan, R.M., Mackay, D.H., Upton, L.A., Riley, P., Lionello, R., Török, T., Titov, V.S., Wijaya, J., Druckmüller, M., Pasachoff, J.M., Carlos, W.:

2018, Predicting the corona for the 21 August 2017 total solar eclipse. *Nature Astronomy* **2**, 913. DOI. ADS.

Morgan, H.: 2011a, Longitudinal Drifts of Streamers across the Heliospheric Current Sheet. *Astrophys. J.* **738**, 190. DOI. ADS.

Morgan, H.: 2011b, The Rotation of the White Light Solar Corona at Height 4 R $_{sun}$ from 1996 to 2010: A Tomographical Study of Large Angle and Spectrometric Coronagraph C2 Observations. *Astrophys. J.* **738**, 189. DOI. ADS.

Morgan, H.: 2015, An Atlas of Coronal Electron Density at 5R$_\odot$. I. Data Processing and Calibration. *Astrophysical Journal, Supplement* **219**, 23. DOI. ADS.

Morgan, H.: 2019, An Atlas of Coronal Electron Density at 5R $_\odot$. II. A Spherical Harmonic Method for Density Reconstruction. *Astrophysical Journal, Supplement* **242**, 3. DOI. ADS.

Morgan, H., Cook, A.C.: 2020, The Width, Density, and Outflow of Solar Coronal Streamers. *Astrophys. J.* **893**, 57. DOI. ADS.

Morgan, H., Druckmüller, M.: 2014, Multi-Scale Gaussian Normalization for Solar Image Processing. *Sol. Phys.* **289**, 2945. DOI. ADS.

Morgan, H., Habbal, S.R., Lugaz, N.: 2009, Mapping the Structure of the Corona Using Fourier Backprojection Tomography. *Astrophys. J.* **690**, 1119. DOI. ADS.

Morgan, H., Habbal, S.R., Woo, R.: 2006, The Depiction of Coronal Structure in White-Light Images. *Sol. Phys.* **236**, 263. DOI. ADS.

Muhamad, J., Kusano, K., Inoue, S., Shiota, D.: 2017, Magnetohydrodynamic Simulations for Studying Solar Flare Trigger Mechanism. *Astrophys. J.* **842**, 86. DOI. ADS.

Nedal, M., Kozarev, K., Zhang, P., Zucca, P.: 2023, Coronal diagnostics of solar type III radio bursts using LOFAR and PSP observations. *Astron. Astrophys.* **680**, A106. DOI. ADS.

Palmerio, E., Luhmann, J.G., Mays, M.L., Caplan, R.M., Lario, D., Richardson, I.G., Whitman, K., Lee, C.O., Sánchez-Cano, B., Wijsen, N., Li, Y., Cardoso, C., Pinto, M., Heyner, D., Schmid, D., Auster, H.-U., Fischer, D.: 2024, Improved modelling of SEP event onset within the WSA-Enlil-SEPMOD framework. *arXiv e-prints*, arXiv:2401.05309. DOI. ADS.

Pesnell, W.D., Thompson, B.J., Chamberlin, P.C.: 2012, The Solar Dynamics Observatory (SDO). *Solar Physics* **275**, 3. DOI. ADS.

Riley, P., Linker, J.A., Lionello, R., Mikic, Z.: 2012, Corotating interaction regions during the recent solar minimum: The power and limitations of global MHD modeling. *Journal of Atmospheric and Solar-Terrestrial Physics* **83**, 1. DOI. ADS.

Schatten, K.H., Wilcox, J.M., Ness, N.F.: 1969, A model of interplanetary and coronal magnetic fields. *Sol. Phys.* **6**, 442. DOI. ADS.

Scherrer, P.H., Schou, J., Bush, R.I., Kosovichev, A.G., Bogart, R.S., Hoeksema, J.T., Liu, Y., Duvall, T.L., Zhao, J., Title, A.M., Schrijver, C.J., Tarbell, T.D., Tomczyk, S.: 2012, The Helioseismic and Magnetic Imager (HMI) Investigation for the Solar Dynamics Observatory (SDO). *Solar Physics* **275**, 207. DOI. ADS.

Schwadron, N.A., Gorby, M., Török, T., Downs, C., Linker, J., Lionello, R., Mikić, Z., Riley, P., Giacalone, J., Chandran, B., Germaschewski, K., Isenberg, P.A., Lee, M.A., Lugaz, N., Smith, S., Spence, H.E., Desai, M., Kasper, J., Kozarev, K., Korreck, K., Stevens, M., Cooper, J., MacNeice, P.: 2014, Synthesis of 3-D Coronal-Solar Wind Energetic Particle Acceleration Modules. *Space Weather* **12**, 323. DOI. ADS.

Török, T., Downs, C., Linker, J.A., Lionello, R., Titov, V.S., Mikić, Z., Riley, P., Caplan, R.M., Wijaya, J.: 2018, Sun-to-Earth MHD Simulation of the 2000 July 14 "Bastille Day" Eruption. *Astrophys. J.* **856**, 75. DOI. ADS.

Vásquez, A.M.: 2016, Seeing the solar corona in three dimensions. *Advances in Space Research* **57**, 1286. DOI. ADS.

Vásquez, A.M., Frazin, R.A., Hayashi, K., Sokolov, I.V., Cohen, O., Manchester, I. Ward B., Kamalabadi, F.: 2008, Validation of Two MHD Models of the Solar Corona with Rotational Tomography. *Astrophys. J.* **682**, 1328. DOI. ADS.

Vibert, D., Peillon, C., Lamy, P., Frazin, R.A., Wojak, J.: 2016, Time-dependent tomographic reconstruction of the solar corona. *Astronomy and Computing* **17**, 144. DOI. ADS.

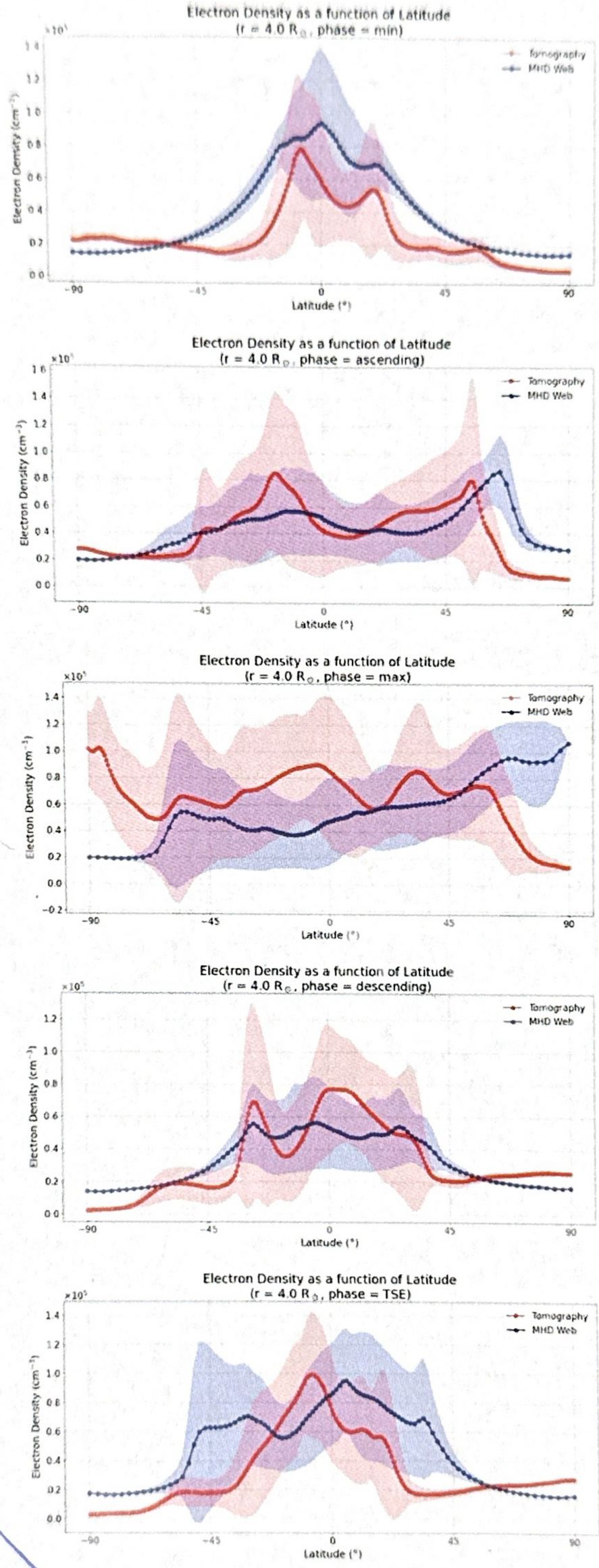


Figure 9. Electron densities derived from the tomography maps (*red*) and MAS model (*blue*) averaged along each latitude for heliocentric heights of 4 $R_\odot$. Both plots show values taken at the same date during each solar cycle phase (see Table 2) and the red and blue shaded areas represent the tomography and MAS model standard deviations, respectively.

better to overlay?

scales are different so difficult to compare

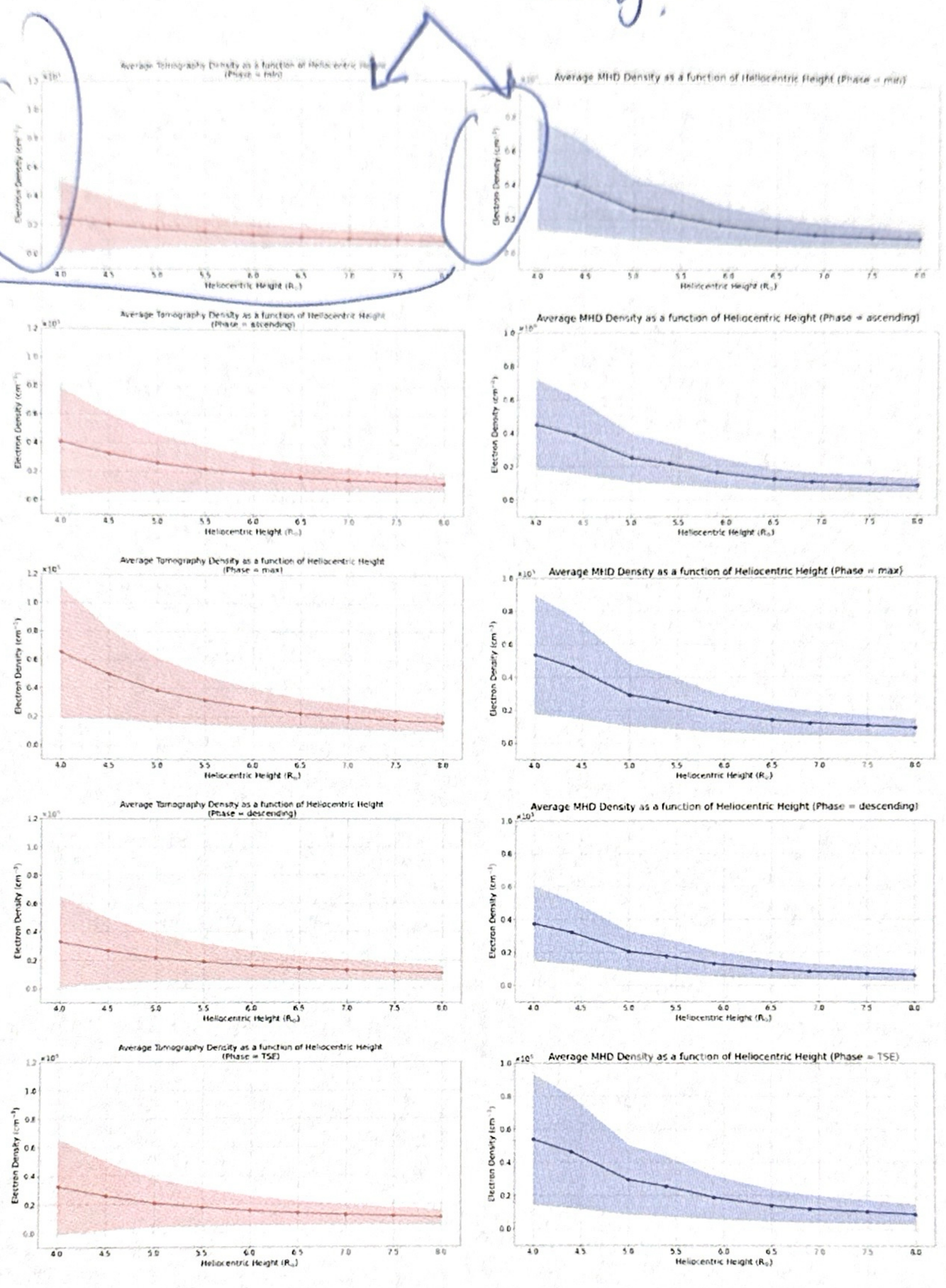


Figure 10. Comparison of average coronal electron densities using tomography (*left column*) and the MAS model (*right column*) as a function of heliocentric height for dates during each phase of the solar activity cycle (*top to bottom*: *minimum*, *ascending*, *maximum*, *descending*, *TSE*). The red and blue shaded regions give the standard deviations of the tomography and MAS model, respectively.

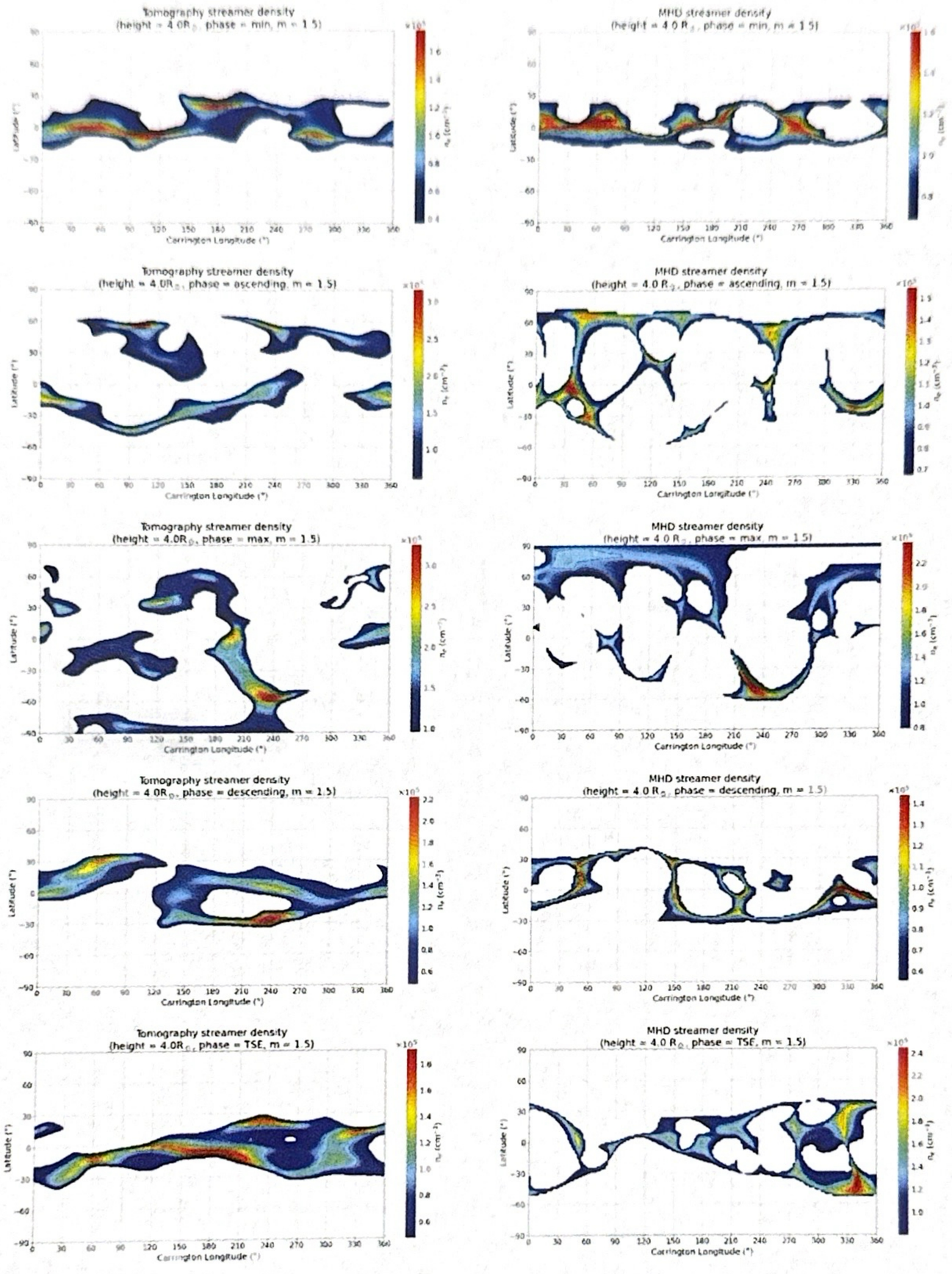


Figure 11. Comparison of streamer electron density maps produced using tomography (*left column*) and the MAS model (*right column*) at a heliocentric height of 4 $R_\odot$ for dates during each phase of the solar activity cycle (*top to bottom*: *minimum*, *ascending*, *maximum*, *descending*, *TSE*).

This is the same data as Fig 4 — doesn't really add anything new - just replaced blue with white!

See comments related to Figure 10

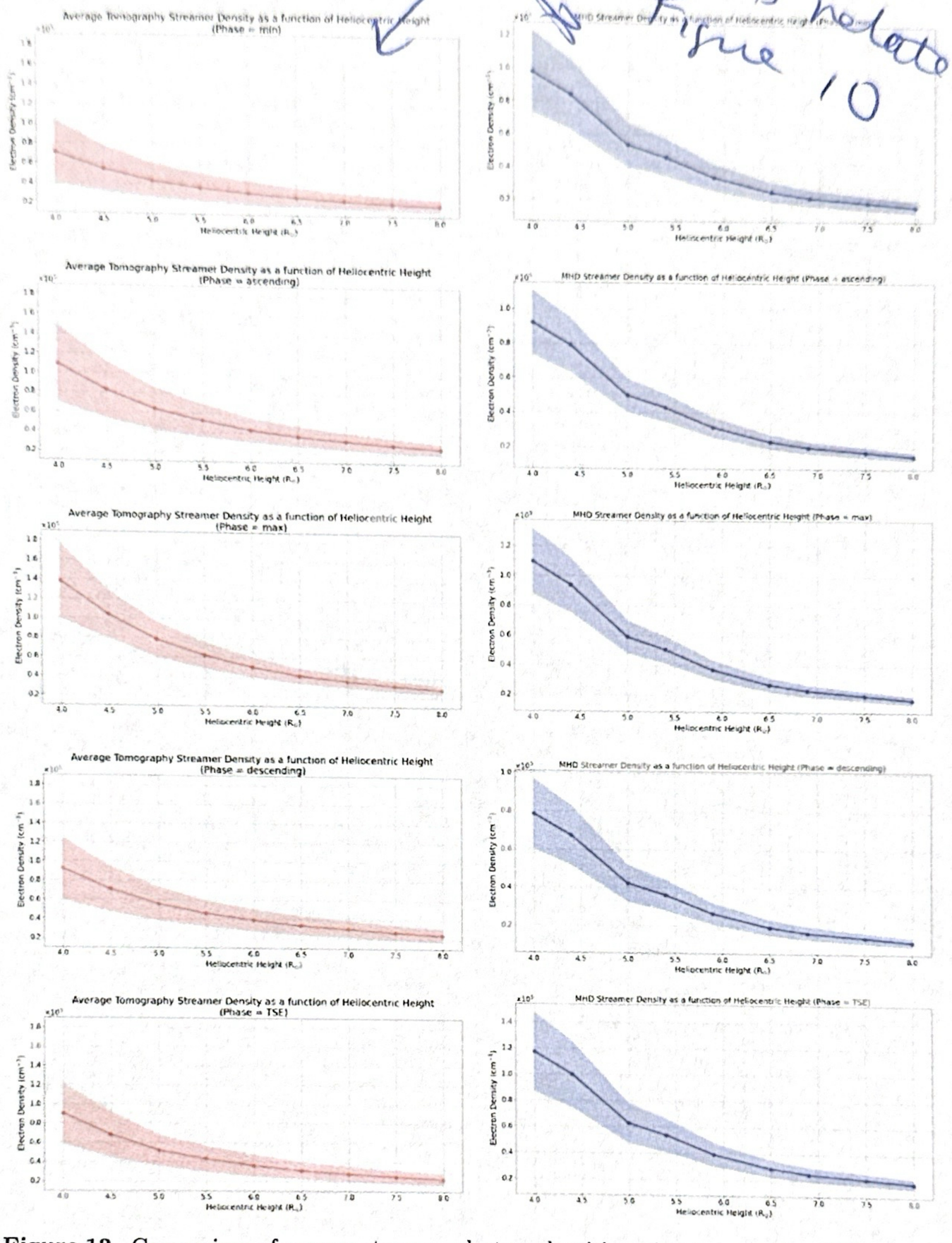


Figure 12. Comparison of average streamer electron densities using tomography (*left column*) and the MAS model (*right column*) as a function of heliocentric height for dates during each phase of the solar activity cycle (*top to bottom*: *minimum*, *ascending*, *maximum*, *descending*, *TSE*). The red and blue shaded regions give the standard deviations of the tomography and MAS model, respectively.

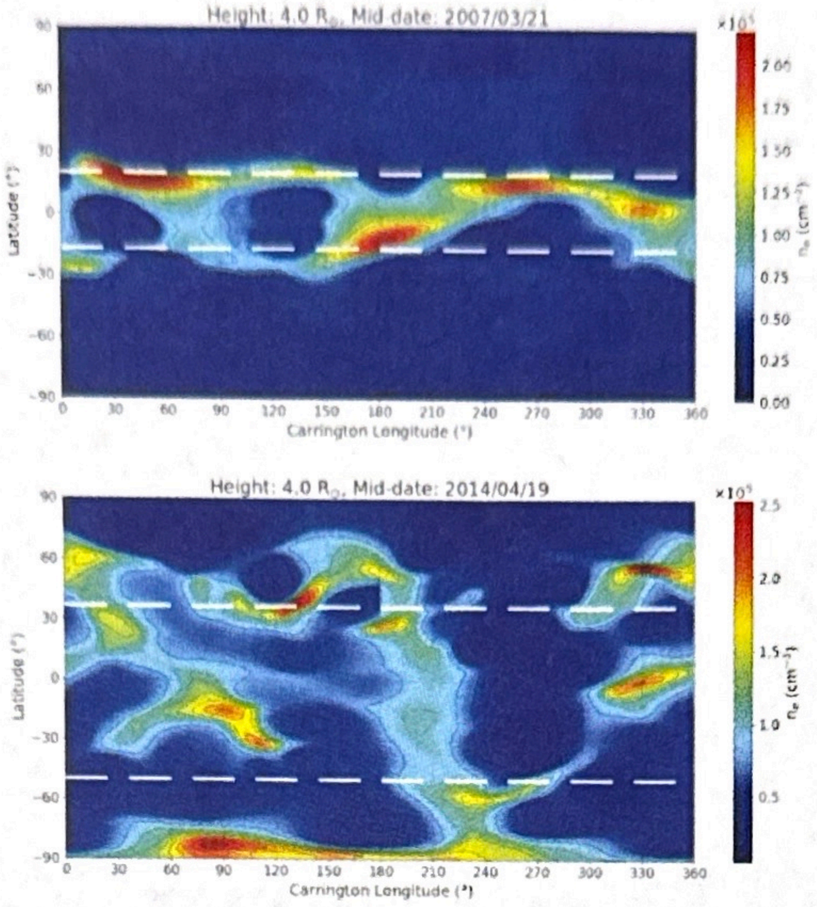


Figure 13. Examples of tomography maps for mid-dates of 21 March 2007 (*top*) and 19 April 2014 (*bottom*) representing periods of minimum and maximum solar activity, respectively. The dashed white lines show the average streamer belt width in each case.

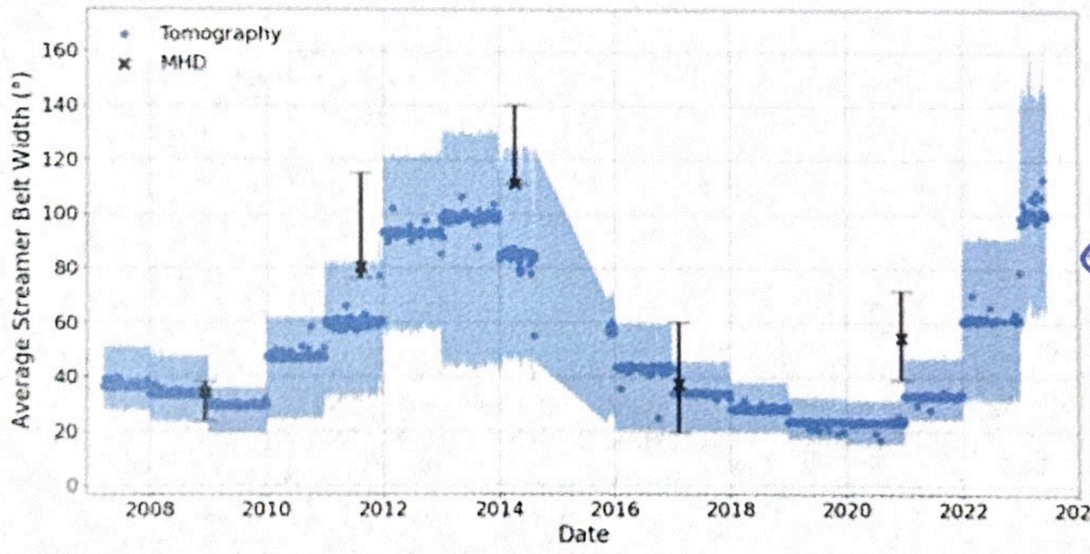


Figure 14. Average streamer belt width calculated for each tomography map available between 2007 and 2022 (blue) with the shaded region representing its standard deviation. The average streamer belt width calculated from the MHD model outputs for each solar cycle phase studied is also shown (black) with corresponding standard deviations shown as vertical error bars. The data gap in the tomography from early 2014 to late 2015 is the data gap as STEREO-A moved behind the sun.

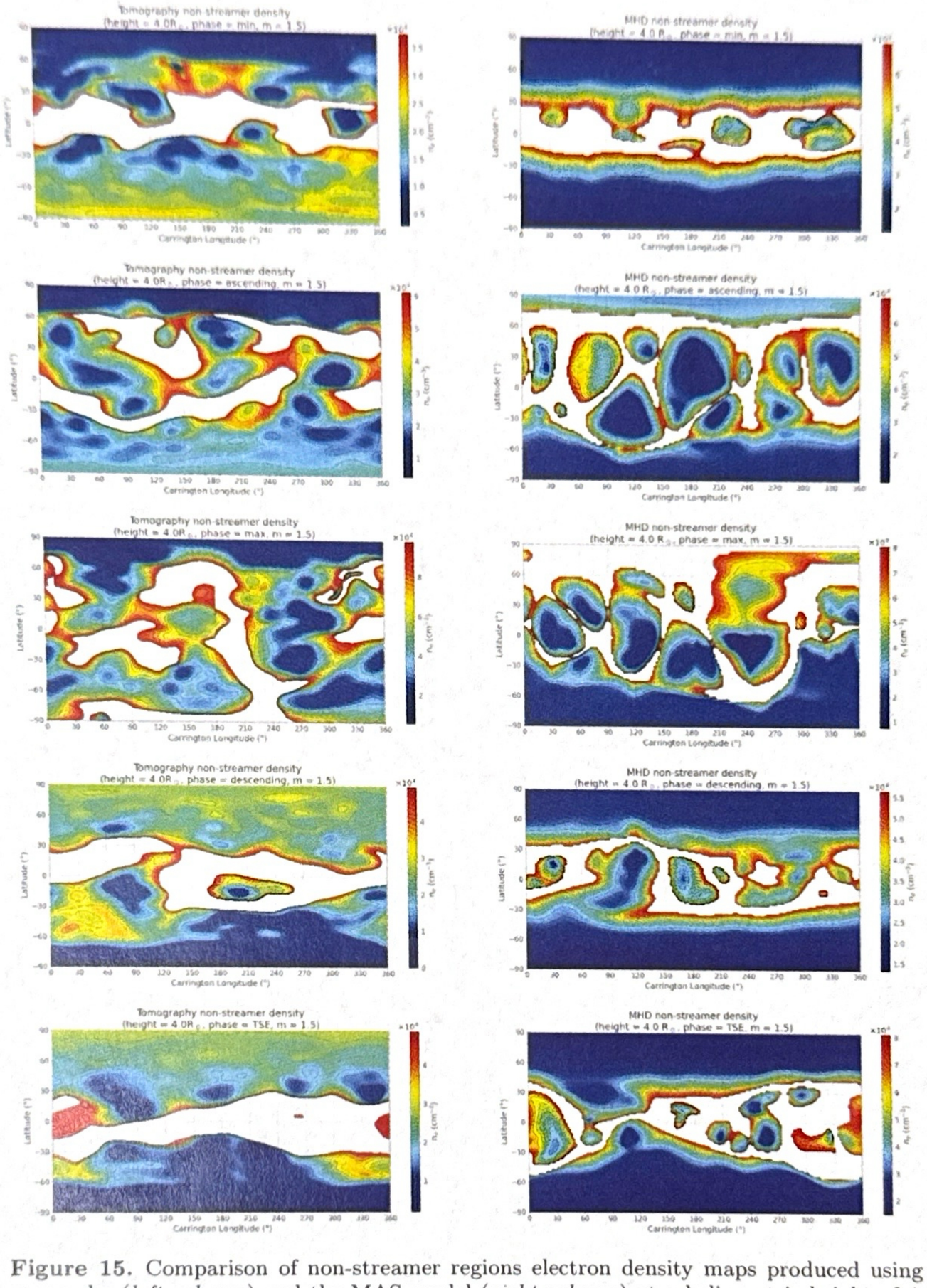


Figure 15. Comparison of non-streamer regions electron density maps produced using tomography (*left column*) and the MAS model (*right column*) at a heliocentric height of 4 $R_\odot$ for dates during each phase of the solar activity cycle (*top to bottom*: *minimum*, *ascending*, *maximum*, *descending*, *TSE*).

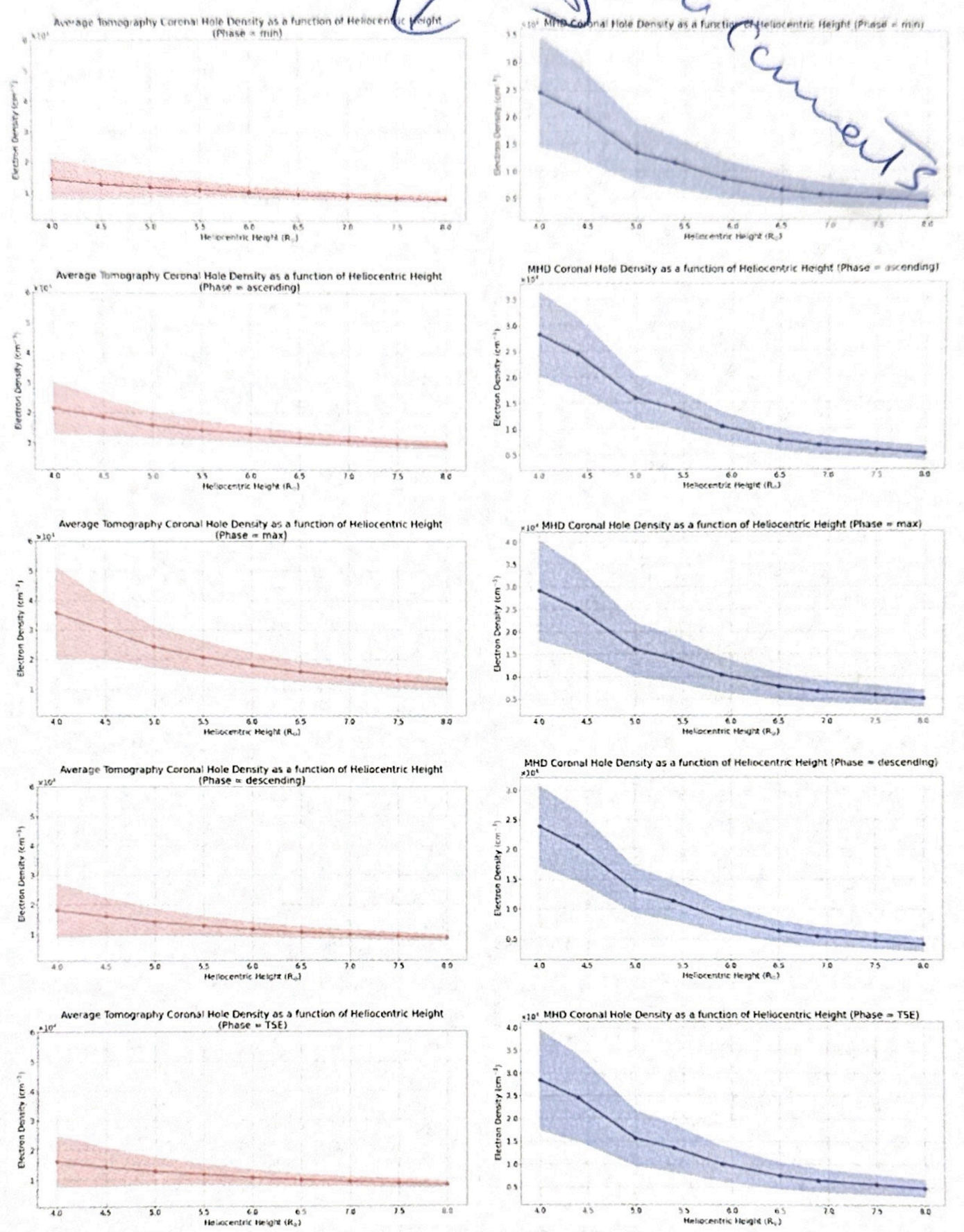


Figure 16. Comparison of average non-streamer electron densities using tomography (*left column*) and the MAS model (*right column*) as a function of heliocentric height for dates during each phase of the solar activity cycle (*top to bottom*: *minimum*, *ascending*, *maximum*, *descending*, *TSE*). The red and blue shaded regions give the standard deviations of the tomography and MAS model, respectively.